pubs.acs.org/acschemicalbiology

Articles

Acylation of MLKL Impacts Its Function in Necroptosis

Apoorva J. Pradhan, Shweta Chitkara, Ricardo X. Ramirez, Viviana Monje-Galvan, Yasemin Sancak, and G. Ekin Atilla-Gokcumen*

Cite This: *ACS Chem. Biol.* 2024, 19, 407−418

Read Online

ACCESS | Metrics & More | Article Recommendations | Supporting Information

ABSTRACT: Mixed lineage kinase domain-like (MLKL) is a key signaling protein of necroptosis. Upon activation by phosphorylation, MLKL translocates to the plasma membrane and induces membrane permeabilization, which contributes to the necroptosis-associated inflammation. Membrane binding of MLKL is initially initiated by electrostatic interactions between the protein and membrane phospholipids. We previously showed that MLKL and its phosphorylated form (pMLKL) are *S*-acylated during necroptosis. Here, we characterize the acylation sites of MLKL and identify multiple cysteines that can undergo acylation with an interesting promiscuity at play. Our results show that MLKL and pMLKL undergo acylation at a single cysteine, with C184, C269, and C286 as possible acylation sites. Using all-atom molecular dynamic simulations, we identify differences that the acylation of MLKL causes at the protein and membrane levels. Through investigations of the *S*-palmitoyltransferases that might acylate pMLKL in necroptosis, we showed that zDHHC21 activity has the strongest effect on pMLKL acylation, inactivation of which profoundly reduced the pMLKL levels in cells and improved membrane integrity. These results suggest that blocking the acylation of pMLKL destabilizes the protein at the membrane interface and causes its degradation, ameliorating the necroptotic activity. At a broader level, our findings shed light on the effect of *S*-acylation on MLKL functioning in necroptosis and MLKL-membrane interactions mediated by its acylation.

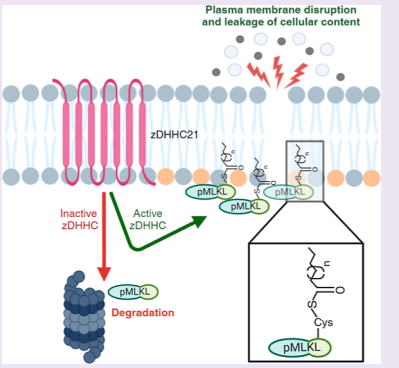

INTRODUCTION

Different types of programmed cell deaths follow complex and interconnected signaling networks and play different roles in cellular homeostasis and pathological conditions.[1,2] Necroptosis is one such type of programmed cell death that is characterized by cell swelling, disruption of plasma membrane, and release of intracellular contents resulting in extensive inflammatory activity.[3,4] Although these morphological characteristics are similar to those in necrosis, which is not regulated, necroptosis has a distinct molecular mechanism. The inflammatory nature of necroptosis is due to membrane rupture and leakage of intracellular contents and is triggered by the activation of the tumor necrosis factor (TNF) receptors via TNF family of cytokines.[5] Binding of TNF alpha (TNFα) to the TNF receptor recruits multiple adaptor proteins, one of which is receptor-interacting protein kinase 1 (RIPK1). This event can signal a cell survival pathway or a cell death pathway, such as apoptosis, when caspase-8 activity is high. The sustained presence of RIPK1 and decreased caspase-8 activity initiate necroptosis where RIPK1 forms a complex with RIPK3, followed by autophosphorylation of RIPK3.[6] This complex results in the phosphorylation of mixed lineage kinase domainlike (MLKL), which then oligomerizes and translocates to the plasma membrane causing membrane rupture. These key interactions that result in the eventual membrane permeabilization make MLKL the executioner protein of necroptosis.[7−10]

MLKL consists of an N-terminal four-helix bundle domain (4HB) with two additional helices (brace domain) connecting the 4HB to the C-terminal pseudokinase domain.[7] The 4HB consists of multiple positively charged amino acids that can interact with the negatively charged phosphatidylinositol phosphates (PIPs) at the plasma membrane.[11,12] This protein−lipid interaction is essential for binding of MLKL to the plasma membrane. The interactions between the C-terminal helix of the brace with the rest of the helices can inhibit the functioning of MLKL in necroptosis.[13] The helices of the brace are responsible for oligomerization of MLKL and also maintain contacts between the 4HB and the pseudokinase domain after phosphorylation, communicating the conformational changes within the pseudokinase domain to the 4HB.[12−14] Works by Wang et al. and Dondelinger et al. have suggested that the membrane disruptive activity of MLKL results from the interactions between the positively charged residues in the 4HB and the negatively charged PIP species present in the membrane leaflet by liposomal models.[8,11] Similarly, Su et al., using reconstituted membranes, have

Received: September 28, 2023
Revised: January 11, 2024
Accepted: January 17, 2024
Published: February 1, 2024

https://doi.org/10.1021/acschembio.3c00603
ACS Chem. Biol. 2024, 19, 407−418

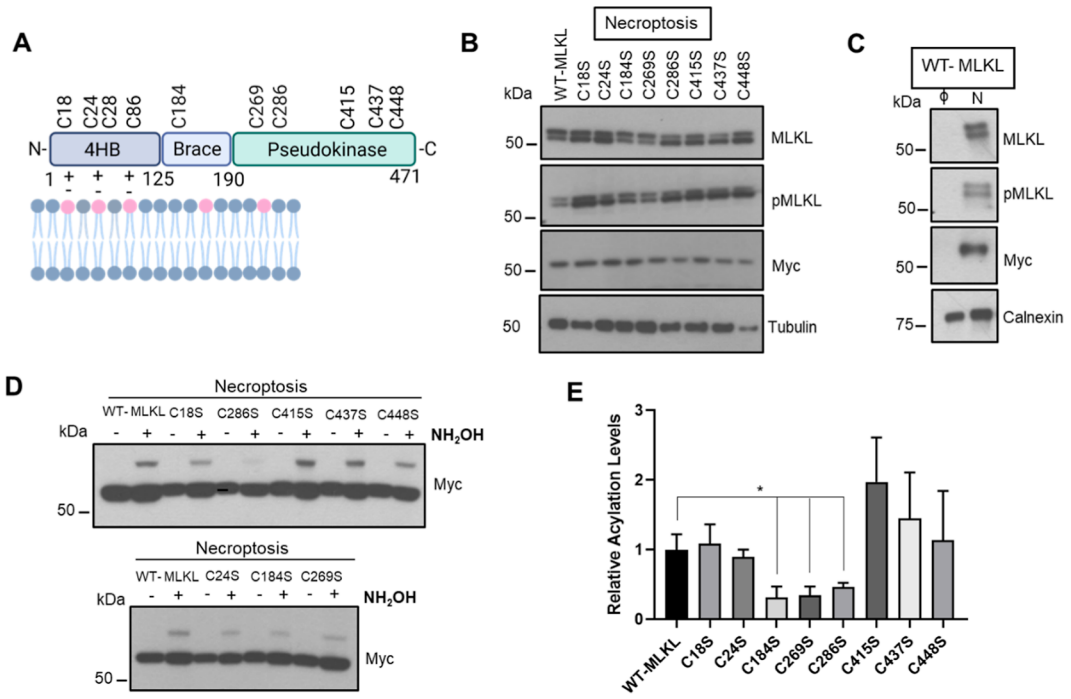

Figure 1. Acylation of cysteines in MLKL. (A) Representation of human MLKL showing the N-terminal 4-helix bundle (4HB) connected to the C-terminal pseudokinase domain via the two helix brace. 4HB spans from amino acid residues 1−125, brace helices up to residue 190, and the pseudokinase domain until residue 471.[20] The positively charged residues in the 4HB interact with the negatively charged PIPs (shown in pink) via electrostatic interactions. The 10 cysteines present in human MLKL and their locations have been shown. Figure created using BioRender. (B) Western blot analysis of Myc-tagged WT-MLKL and the 8 constructs with C to S mutations. Necroptosis was induced in HT-29 cells following treatment with 1 μM BV6, 25 μM zVAD-fmk, and 10 ng/μL TNFα and collected after 3 h. Each of the constructs expresses the Myc-tagged MLKL and also undergoes necroptosis. MLKL and pMLKL show up as two bands, with the Myc-tagged form being the top band and endogenous forms being the bottom bands. (C) WT-MLKL control and necroptotic cells were treated with C20 alkFA and fractionated. The membrane fraction was subjected to CuAAC to attach biotin-azide, followed by enrichment on the neutravidin resin. The samples were blotted for MLKL, pMLKL, and Myc. Calnexin was used as a loading control. (D) C184S, C269S, and C286S show profound reduction in acylation as compared to WT-Myc in necroptosis. Acyl PEG exchange with *N*-ethylmaleimide (NEM), hydroxylamine (NH_2OH), and methoxypolyethylene glycol maleimide (mPEG-Mal) was performed on necroptotic WT-MLKL and cysteine mutant cells. The conditions without NH_2OH (represented by −) are controls for the presence of acylation. The samples are blotted for myc. (E) Quantification of the extent of acylation for C18S, C24S, C184S, C269S, C286S, C415S, C437S, and C448S with respect to control WT-MLKL. The extent of acylation is calculated by dividing the background-subtracted intensities of migrated Myc-tagged MLKL relative to nonmigrated Myc-tagged MLKL for WT-MLKL and the mutants (using Fiji). The relative values are calculated by normalizing values for the mutants with respect to the values obtained for Myc-tagged WT-MLKL. Data represent the mean ± 1 SD; $n = 3$. * represents $p < 0.05$.

suggested that the 4HB can directly insert into the membranes, causing membrane disruption.[13]

The C-terminal of MLKL is a pseudokinase.[7] Multiple studies implicate the pseudokinase domain functioning as a "switch" to regulate necroptotic signaling, downstream of MLKL phosphorylation with several charged residues within the domain essential for driving the oligomerization and translocation to the plasma membrane.[15,16] A study elucidated the sequence of MLKL activation by proposing a model of initial dimerization of the pseudokinase domain after phosphorylation by RIP3 followed by oligomerization via the brace region.[17] Overall, the functioning of MLKL as the executioner of necroptosis involves multiple steps and dynamic changes that warrant further investigations.

Previous studies from our laboratory revealed additional protein-membrane interactions that mediate MLKL binding to the plasma membrane during necroptosis. We showed that MLKL and pMLKL are *S*-acylated by very long-chain fatty acids (fatty acids with ≥20 carbons[18]) during necroptosis and that this acylation increases their membrane binding and exacerbates membrane permeabilization in this process.[19] However, the biochemical characterization of MLKL acylation and, importantly, the implications of acylation on MLKL functioning in necroptosis remained unknown. In this work, we first studied the cysteines that can be possible targets of acylation in necroptosis. Using all-atom molecular dynamics simulations, SwissPalm predictions, and cysteines with previously unaccounted functions, we prioritized cysteines that are likely to interact with the lipid bilayer because palmitoyl transferases are membrane associated. Mutagenesis experiments followed by acyl-PEG exchange (APE) suggested that C184, C269, and C286 can undergo acylation in necroptosis. We then characterized the involvement of plasma membrane-localized palmitoyl transferases in the acylation of MLKL and pMLKL during necroptosis. We demonstrate that zDHHC21 activity has the most profound effect on the MLKL and pMLKL acylation. Inactivating zDHHC21 disrupted the acylation of pMLKL, ameliorated plasma membrane disruption, and, intriguingly, decreased the overall levels of pMLKL, most likely through increased protein degradation. Altogether, these results provide new insights into the interactions that regulate the role of pMLKL in necroptosis.

https://doi.org/10.1021/acschembio.3c00603
ACS Chem. Biol. 2024, 19, 407−418

RESULTS

C184, C269, and C286 of MLKL Are Acylated in Necroptosis. Our previous efforts to understand protein acylation in necroptosis showed that MLKL and pMLKL undergo a mono *S*-acylation during necroptosis downstream of plasma membrane translocation.[19] The human MLKL has 10 cysteines across the 4HB, the brace, and the pseudokinase domain, with C18, C24, C28, and C86 within the 4HB; C184 in the brace helix and C269, C286, C415, C437, and C448 within the pseudokinase domain (Figure 1A).[20] The four cysteines in the 4HB, C18, C24, C28, and C86 are involved in oligomerization of MLKL and induction of necroptosis.[10] Hence, they are likely buried in the oligomerization interface and not available for interactions with palmitoyl transferases located at the plasma membrane. Further, studies report that C86 is the target residue of necrosulfonamide, which inhibits MLKL oligomerization,[21,22] suggesting that C86 is not likely to interact with the plasma membrane and be available for acylation.

We first used all-atom molecular dynamic simulations to investigate the interaction of murine MLKL with a membrane model based on the lipid content of HT-29 cells.[23] The simulations identified different protein-bound conformations with the 4HB or the pseudokinase domain interacting with the lipid membrane; the 4HB was found to have deeper membrane insertion, in agreement with previously published reports of the 4HB being responsible for contact with the lipid membrane and subsequent insertion.[13] The trajectories showing interactions of the pseudokinase domain with the membrane resulted in a different lipid landscape around the protein after the simulation reached equilibrium.[23] Upon further examination of these trajectories, we observed C23, C379, C280, and C407 consistently have the highest occupancy in terms of percentage of time bound to the membrane (Table S1, highlighted in green), suggesting that they might interact with membrane-bound enzymes. The corresponding cysteines in human MLKL were then selected for further investigations ($C18_{human} \rightarrow C23_{murine}$, $C286_{human} \rightarrow C280_{murine}$, $C415_{human} \rightarrow C407_{murine}$; and $Y387_{human} \rightarrow C379_{murine}$ in MLKL, Figures 1A and S1A). In parallel, we consulted with the SwissPalm database[24,25] which predicts C18 and C24 to be palmitoylated. The remaining cysteines, C184, C269, C437, and C448, do not have any known role in MLKL functionality in necroptosis, warranting investigations in their involvement in acylation. Based on these analyses, we shortlisted C18, C24, C184, C269, C286, C415, C437, and C448 to be investigated for their role in acylation in necroptosis.

We conducted mutagenesis studies to investigate the involvement of the cysteines mentioned above in pMLKL and MLKL acylation during necroptosis. We first subcloned a commercially available MLKL sequence in a pLYS1 vector expressing a Myc tag and introduced point mutations to generate $MLKL_{C18S}$, $MLKL_{C24S}$, $MLKL_{C184S}$, $MLKL_{C269S}$, $MLKL_{C286S}$, $MLKL_{C415S}$, $MLKL_{C437S}$, and $MLKL_{C448S}$ constructs. These were then used to generate lentiviruses to transduce HT-29 cells and express Myc-tagged WT MLKL (WT-MLKL) and mutant forms of MLKL. We confirmed the expression of WT-MLKL and mutant forms and the ability of the HT-29 cells expressing Myc-tagged MLKL forms to undergo necroptosis by Western blotting (Figure 1B). Briefly, we induced necroptosis using BV6, a SMAC mimetic and a pan-caspase inhibitor zVAD-FMK followed by TNF-α as we described previously.[19,26,27] We collected cells after 3 h of necroptosis induction, and samples were analyzed using Western blotting. The two bands in Figure 1B correspond to the endogenous MLKL (lower band, MW: ∼55 kDa) and the Myc-tagged MLKL (upper band, MW: ∼57 kDa). The generation of functional Cys to Ser mutants capable of undergoing necroptosis was supported by the expression of MLKL and pMLKL in both the WT and mutant forms of MLKL (Figure 1B). We further confirmed the ability of Myc-tagged WT-MLKL to undergo acylation during necroptosis by using a clickable C20 FA probe (Figure 1C). These results established that Myc-tagged MLKL can undergo acylation, similar to that of the endogenous MLKL in necroptosis.

We then used APE to study the role of these cysteines in the extent of acylation of MLKL. APE involves removing the acyl chains on modified cysteines with hydroxylamine to generate free sulfhydryl groups and then tagging these sulfhydryl groups with a high-molecular-weight polyethylene glycol (PEG), which introduces a mass shift that can be observed using SDS−PAGE.[28] This allows us to calculate the extent of acylation for the mutants by comparing the levels of acylated Myc-tagged MLKL to the level of nonacylated Myc-tagged MLKL expressed in the cells, for control WT-MLKL and each of the mutants. We observed that three mutant forms of MLKL, $MLKL_{C184S}$, $MLKL_{C269S}$, and $MLKL_{C286S}$, showed a significant decrease ($p < 0.05$, *t*-test) in acylation as compared to WT-MLKL, while $MLKL_{C18S}$, $MLKL_{C24S}$, $MLKL_{C415S}$, $MLKL_{C437S}$, and $MLKL_{C448S}$ remained unaffected (Figure 1D,E). Specifically, C184S and C269S mutations resulted in a 68 and 65% reduction, whereas C286S mutation showed a 53% reduction in acylation of MLKL-Myc. We note that the C24S mutant also showed ∼20−30% reduction in acylation, but this reduction was not statistically significant ($p > 0.05$).

Our previous results consistently showed a single band of mass shift for acylated MLKL in APE experiments, suggesting that, predominantly, a single cysteine residue of MLKL is acylated and that multiple acylations on the sample protein are not applicable during necroptosis.[19] However, our mutagenesis results point to a preference of three cysteines, C184, C269, and C286, as acylation sites. C184 is situated in the brace helix of MLKL, with the other two cysteines in the pseudokinase domain[20] with the brace in mouse MLKL found to interact with membrane lipids.[29] This observation points to a mechanism where acylation of either of the three cysteines during necroptosis locks the protein in a specific conformation at the membrane surface upon insertion of the acylated tail, with the other two cysteines being unmodified.

Acylated MLKL Interacts with Membrane Lipids. We previously conducted all-atom simulations of a complex membrane model composed of a mixture of 5 lipid species [dioleoyl-phosphatidylcholine (DOPC), dioleoyl-phosphatidylethanolamine (DOPE), cholesterol, palmitoyl-oleoyl-phosphatidylinositol 4-phosphate (PIP), and palmitoyl-oleoyl-phosphatidylinositol (2,5)-bisphosphate (PIP_2)] with the murine MLKL protein (PDB ID: 4BTF).[23] We showed that MLKL interacts with membrane lipids and leaves a specific fingerprint on the membrane local composition upon binding. Here, we used a similar approach to investigate acylated MLKL-membrane interactions and compared those to that of nonacylated MLKL. Our simulations comprised an *S*-acylated MLKL with C24 FA (a representative very long-chain fatty acid) at C286 (residue 280 in murine MLKL), as a model acylation site, based on the mutagenesis results presented in

https://doi.org/10.1021/acschembio.3c00603
ACS Chem. Biol. 2024, 19, 407−418

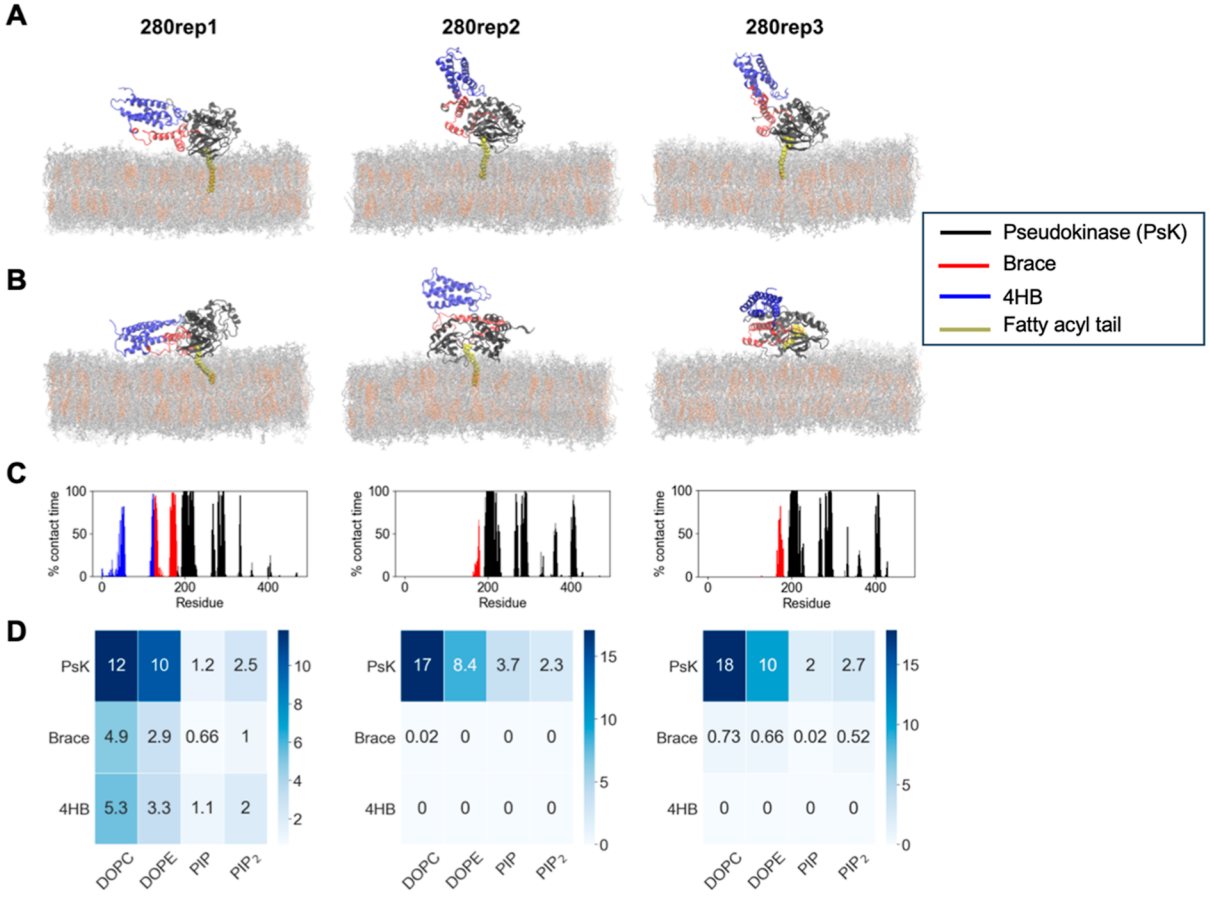

Figure 2. Molecular dynamics shows interaction of acylated MLKL with membrane lipids. (A) Position of the protein in the membrane after 50 ns of equilibration, initial interaction; (B) after 1050 ns of simulation; (C) frequency of contact of each residue in the protein during the simulation; and (D) mean lipid distribution of the lipids within 12 Å of the protein for the last 200 ns of simulation.

Figure 1, and the same membrane model we describe in the previous section. We simulated a total of three replicas referred to as 280r1, 280r2, and 280r3 (Figure 2) and characterized protein−lipid interactions in acylated vs nonacylated MLKL to assess the effect of acylation in MLKL-membrane interactions.

Figure 2A,B shows the protein starting from a bound conformation with the acylated tail partially or fully inserted into the membrane and the final bound conformations, respectively. The lipid tail remains inserted during the full trajectory for 280r1 and 280r2, whereas it reverts to a hydrophobic pocket in the protein around 250 ns in replica 280r3. The most striking difference between the acylated system (Figure 2) and that of the endogenous MLKL[23] is the conformational change of the protein in 280r2 and 280r3 (Figure S2). In these replicas in the acylated MLKL, 4HB (shown in blue) shifts its original position and aligns with the brace in a parallel fashion (shown in red), which did not occur in the nonacylated version. In all of our simulation trajectories, we observe characteristic profiles for the protein−lipid frequency of contact depending on the specific protein domain that interacts with the membrane (Figure 2C). The conformational changes observed in the 4HB and brace conformational changes appear to result from the insertion and interaction of the acyl tail with other membrane lipids (Figure 2D).

When inserted into the membrane, the 24-carbon acyl tail behaves like other lipids in the membrane and influences the lateral distribution of lipids nearby, which, in turn, modulates protein conformational changes on the surface. These conformational changes can result in the acyl tail returning to the membrane surface as shown in 280r3 (Figure S3D). Insertion dynamics of the protein acyl tail are affected by (i) the conformational changes of the protein on the membrane surface, (ii) the lipid environment that surrounds it, or (iii) a combination of both. We note that in the physiological system, the protein units can survey the membrane surface and permanent insertion of the lipid tail occurs in the most suitable lipid environment. Similar observations have been reported for other lipidated proteins.[30−32] The lipid environment within 15 Å of the acyl tail in 280r1, compared to the other replicas, is enriched in cholesterol (Figure S3A−C), which is known to induce an ordered structure in the membrane hydrophobic core. Furthermore, 280r1 shows the deepest and more stable insertion of the acyl tail into the membrane core, suggesting that cholesterol-enriched regions facilitate stable insertion of the protein acyl tail. On the other hand, the protein acyl tail in 280r3 exits the membrane as shown by the position of its methyl group with respect to the bilayer center (Figure S3D). This process may be a result of both conformational changes in the protein and low cholesterol concentration in the immediate environment. It is plausible that a more saturated local lipid environment, as would result upon enrichment of VLCFAs and cholesterol, could provide a more stable insertion of the acyl tail and recruitment of additional MLKL units and promote membrane disruption.

To examine the influence of the protein-bound conformation and acylation on the internal structure of the membrane,

https://doi.org/10.1021/acschembio.3c00603
ACS Chem. Biol. 2024, 19, 407−418

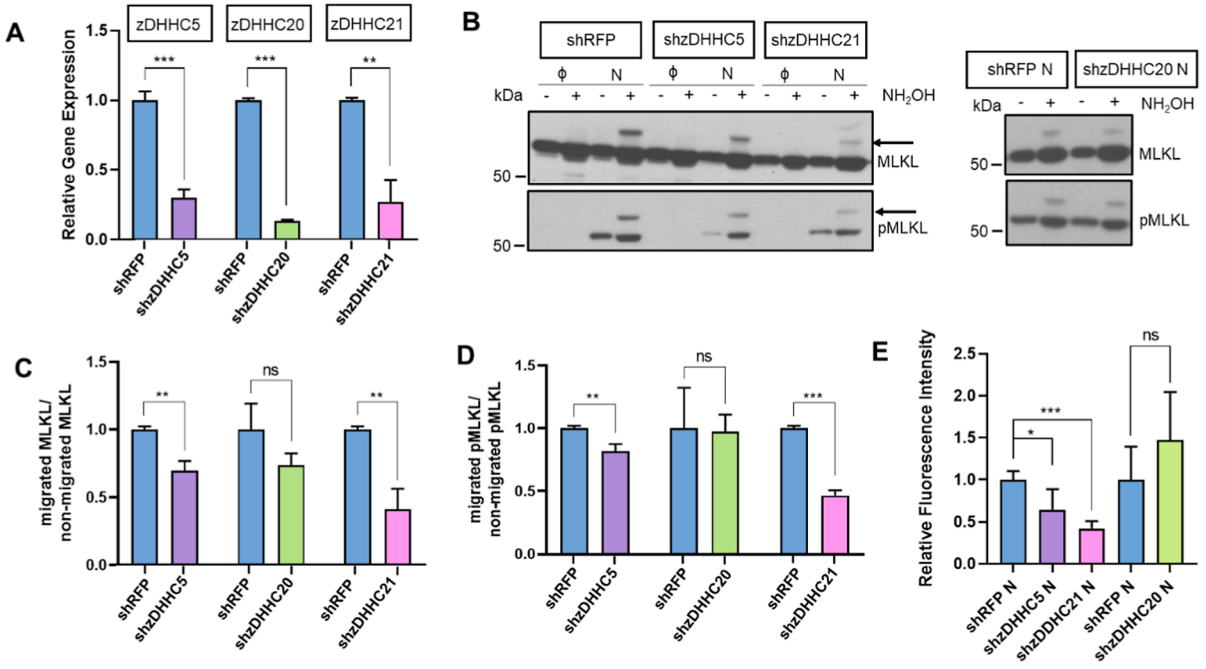

Figure 3. zDHHC21 has the largest effect in regulating acylation of MLKL and pMLKL in necroptosis. (A) Gene expression levels indicating knockdown of zDHHC5, zDHHC21, and zDHHC20. We knocked down zDHHC5, zDHHC21, and zDHHC20 using a lentiviral shRNA vector in HT-29. Relative gene expression levels are calculated as the ratio of expression level of each target gene compared to the control HPRT1 expression levels. Data represent mean ± 1 SD; $n = 3$. ** represents $p < 0.01$, *** represents $p < 0.001$. (B) Acyl PEG exchange with NEM, NH_2OH, and mPEG-Mal in the control and necroptotic shRFP, shzDHHC5, shzDHHC20, and shzDHHC21 cells. (C) Quantification of acylated MLKL in shzDHHC5, shzDHHC20, and shzDHHC21 compared to shRFP. The ratio is calculated by dividing migrated band intensities of MLKL with nonmigrated band intensities. Data represent mean ± 1 SD; $n = 3$. ** represents $p < 0.01$, *** represents $p < 0.001$. (D) Quantification of acylated pMLKL in shzDHHC5, shzDHHC20, and shzDHHC21 compared to shRFP. The ratio is calculated by dividing migrated band intensities of pMLKL with nonmigrated band intensities. Data represent mean ± 1 SD; $n = 3$. ** represents $p < 0.01$ and *** represents $p < 0.001$. (E) zDHHC knockdown affects membrane permeabilization. Relative fluorescence intensity represents the propidium iodide uptake of shzDHHC cells compared to control shRFP cells in necroptosis. Data represent mean ± 1 SD; $n = 4$. ns represents $p > 0.05$, * represents $p < 0.05$, and *** represents $p < 0.001$.

we investigated the splay angle of each lipid species (Figure S4). We report the average angle between the fatty acid tails of lipids underneath the protein site, which provides insights on the local spatial changes of membrane lipids upon protein binding. Figure S4A shows a general trend of lower splay angle when the protein is acylated (280r1−280r3) compared to higher angles for the membranes with a nonacylated protein (Rep1-Rep4), reported previously.[23] Furthermore, Figure 4E shows the splay angles of PIP and PIP_2 lipids in the binding leaflet (blue bars) are also smaller than the angles between the fatty acid tails in the nonbinding leaflet (orange bars) when the acylated protein interacts with the membrane. The opposite trend is observed, in general, for the splay angles of lipids under the nonacylated protein. This indicates a preference for a closed conformation for the fatty acid tails of individual lipids right underneath the acylated protein, especially when a VLCFA is present, yet an opposite response in the lipids in the nonbinding leaflet. It is plausible that this local rearrangement of lipid tail conformation increases as more protein units oligomerize at the membrane interface during necroptosis, resulting in lipid platforms with markedly different physical properties than the surrounding membrane. Such changes in the lateral packing of lipid tails could also affect membrane permeabilization.

zDHHC21 Is the Major Regulator of MLKL Acylation. We have previously shown that the acylation of MLKL occurs at the plasma membrane downstream to its phosphorylation and oligomerization and that zDHHC5 plays a role in the acylation of MLKL in necroptosis.[19] Specifically, inactivating zDHHC5 reduced the level of acylation of MLKL and pMLKL but did not completely block it, suggesting that there might be other acyltransferases at the plasma membrane that are involved in the acylation of MLKL and pMLKL during necroptosis.

The zDHHC family of palmitoyl transferases consists of 23 members residing mainly at the endoplasmic reticulum and Golgi with a few localized to the plasma membrane and the mitochondria.[33] These enzymes can exhibit a certain degree of substrate specificity, although some redundancies have also been observed. Based on the promiscuity and multiple domains impacting substrate recognition, it is difficult to predict the protein substrate specificity of zDHHCs using bioinformatic tools. Here, to investigate the involvement of zDHHC enzymes in the acylation of MLKL and pMLKL in necroptosis, we first used a pan-zDHHC inhibitor, 2-bromo palmitate and tested its effect on acylation during necroptosis. 2-Bromo palmitate treatment reduced the levels of acylated MLKL and pMLKL during necroptosis (Figure S5, $p < 0.01$), consistent with the involvement of zDHHC family of enzymes in MLKL and pMLKL acylation in this process. We then focused on zDHHC members that have been reported to localize at the plasma membrane, including zDHHC5, zDHHC20 and zDHHC21.[34−37] We confirmed that these zDHHCs are indeed expressed in HT-29, our model cell line of necroptosis.[26] We then knocked down zDHHC5 (as a condition known to impact acylation[19]), zDHHC20 and

https://doi.org/10.1021/acschembio.3c00603
ACS Chem. Biol. 2024, 19, 407−418

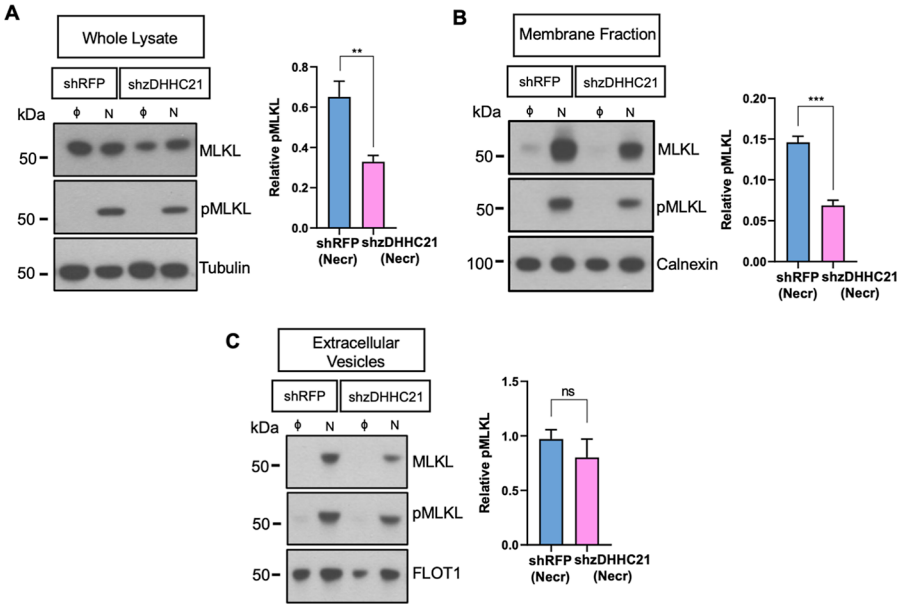

Figure 4. zDHHC21 regulates pMLKL levels during necroptosis. (A) shzDHHC21 has decreased levels of pMLKL present in the cells during necroptosis. Control and necroptotic shRFP and shzDHHC21 whole lysates were normalized based on protein amounts. The samples were blotted for MLKL and pMLKL. Tubulin was used as the loading control. The bar plot represents the quantification of Western blot. The relative pMLKL to total MLKL levels were calculated by dividing the corrected intensities of pMLKL (normalized to tubulin) with respective normalized MLKL. Normalized MLKL for shRFP and shzDHHC21 was calculated by dividing the corrected intensities of MLKL (normalized to tubulin) with the average corrected MLKL band intensities in the shRFP or shzDHHC21 control. (B) shzDHHC21 cells have decreased pMLKL levels present at the membrane during necroptosis. Control and necroptotic shRFP and shzDHHC21 cells were fractionated and normalized based on protein amounts. The samples were blotted for MLKL and pMLKL. Calnexin was used as the loading control. The bar plot represents the quantification for the Western blot. The relative pMLKL to total MLKL levels were calculated by dividing the corrected intensities of pMLKL (normalized to calnexin) with respective normalized MLKL. Normalized MLKL for shRFP and shzDHHC21 was calculated by dividing the corrected intensities of MLKL (normalized to calnexin) with the average corrected MLKL band intensities in shRFP or shzDHHC21 control. (C) Levels of pMLKL released from shzDHHC21 and shRFP cells remained unchanged during necroptosis. The bar plot represents relative pMLKL levels released by necroptotic shzDHHC21 and shRFP cells. The samples were normalized based on protein amounts and samples blotted for pMLKL and FLOT1. Plot represents relative protein levels calculated by normalizing the corrected intensities for pMLKL with the corrected intensities for FLOT1. Data represent mean ± 1 SD; $n = 3$. ** represents $p < 0.01$ and *** represents $p < 0.001$.

zDHHC21 using shRNA (Figure 3A, shzDHHC5, shzDHHC20, shzDHHC21; shRFP was used a negative control), with 70−90% efficiency (Figure 3A). We then investigated the effect of reduced zDHHC activities on the acylation of MLKL and pMLKL in necroptosis using APE. We induced necroptosis in shzDHHC5, shzDHHC20, shzDHHC21, and shRFP cells. We compared the intensities of nonacylated-MLKL and -pMLKL (lower band) and their acylated form (migrated, upper bands, indicated by black arrows, Figure 3B). We quantified the difference in acylation between the knockdowns by calculating the ratios of the migrated band intensities of MLKL and pMLKL with the respective nonmigrated band intensities. As expected, we observed a significant decrease in acylation of MLKL and pMLKL in shzDHHC5 (30 and 18%, respectively). Interestingly, the inactivation of zDHHC21 had a stronger effect on acylation (60 and 55% reduction for MLKL and pMLKL, $p < 0.05$) during necroptosis (see Figure 3B for a representative Western blot image; quantifications of Western blots are shown in Figure 3C,D). The knockdown of zDHHC20 had no effect on acylation of MLKL and pMLKL (Figure 3C,D, $p > 0.05$, *t*-test) in necroptosis, albeit efficient knockdown levels (Figure 3A). Consistent with the extent of reductions in acylation, inactivating zDHHC21 resulted in a strong decrease in the PI uptake (~60%, $p < 0.001$, compared to 40% in shzDHHC5 cells, $p < 0.05$) while the knockdown of zDHHC20 had no appreciable effect on membrane permeability in necroptotic cells as compared to control counterparts (Figure 3E). Based on these results combined, we propose that the reduction in the PI uptake in shZDHHC21 cells is due to reduced MLKL acylation; however, we cannot exclude potential involvement of other zDHHC21 substrates either in an MLKL-dependent or -independent manner. Overall, these results show that while multiple zDHHCs can acylate MLKL and pMLKL, among the members we tested, zDHHC21 has the most profound effect on their acylation during necroptosis and contributes to the membrane permeabilization in this process.

Reducing Acylation Impacts Cellular Levels of pMLKL during Necroptosis. Our results demonstrate that reducing MLKL and pMLKL acylation via zDHHC21 inactivation restores membrane integrity during necroptosis (Figure 3E). Previous studies showed that zDHHC21 depletion ameliorated septic injury in renal reperfusion[38] and barrier dysfunction in endothelial inflammation,[39] suggesting an important role for zDHHC21 in membrane integrity. Based on these, we decided to focus on the involvement of zDHHC21 in the fate of pMLKL, the functional form of MLKL in necroptosis. We induced necroptosis in shzDHHC21 and shRFP cells and analyzed pMLKL levels using Western blotting. To account for any changes in basal expression of MLKL due to zDHHC21 knockdown, we quantified pMLKL levels relative to the total MLKL level. We observed ~50% decrease ($p < 0.01$) in total pMLKL present in the lysate (Figures 4A and S6A) and 53%

https://doi.org/10.1021/acschembio.3c00603
ACS Chem. Biol. 2024, 19, 407−418

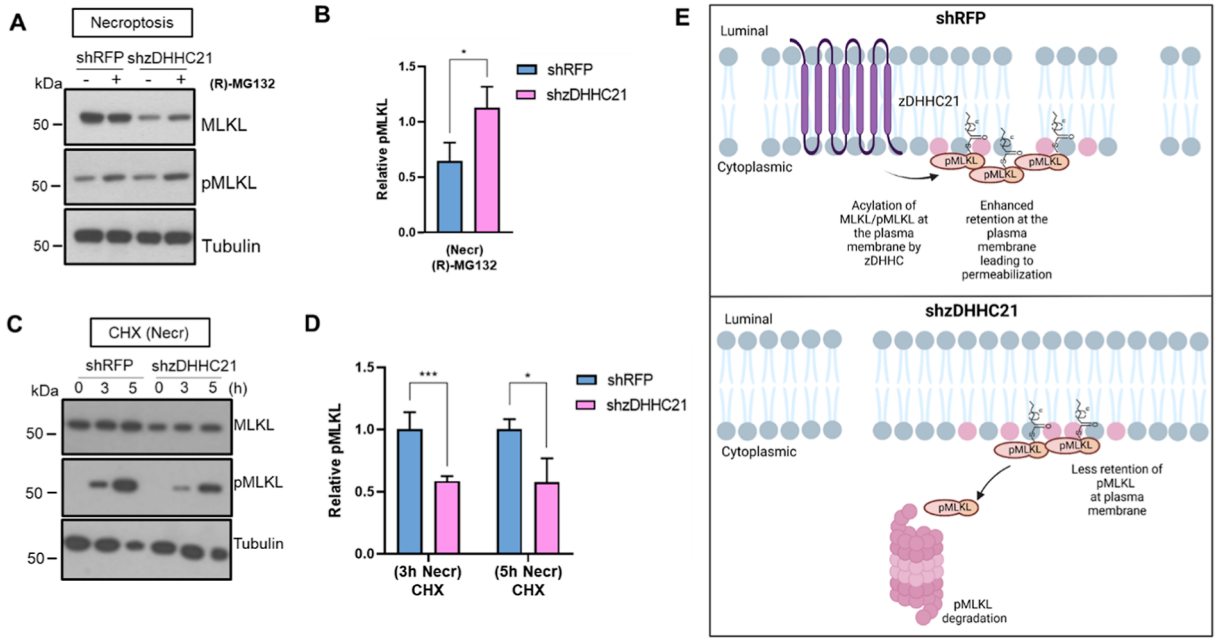

Figure 5. zDHHC21-mediated acylation regulates pMLKL stability during necroptosis. (A) Western blot of the cytosolic fraction of shzDHHC21 and shRFP cells after (*R*)-MG132 treatment. Cells were pretreated with 10 μM (*R*)-MG132 for 24 h, followed by 3 h of necroptosis. Cells were fractionated to obtain the cytosolic proteins. Samples were blotted for MLKL and pMLKL. Tubulin was used as a loading control. (B) Relative pMLKL levels calculated by dividing the corrected intensities of pMLKL (normalized to tubulin) with respective normalized MLKL. Normalized MLKL for shRFP and shzDHHC21 was calculated by dividing the corrected intensities of MLKL (normalized to tubulin) with the average corrected MLKL band intensities in shRFP or the shzDHHC21 control. (C) Western blot analysis of shRFP and shzDHHC21 in the presence of 300 μg/mL of cycloheximide (CHX). Samples were collected at 0, 3, and 5 h postnecroptosis induction and prepared for Western blotting. Samples were blotted with MLKL, pMLKL, and tubulin. (D) Quantification of pMLKL in shzDHHC21 relative to shRFP at 3 and 5 h postnecroptosis. The relative intensities are calculated by dividing the corrected intensities of each protein with the corrected intensities of tubulin and normalizing them to the necroptotic shRFP control. MLKL in necroptosis as a way to limit cell death before being overcome with the death signal. Loss of zDHHC21 results in less retention of pMLKL at the plasma membranes due to reduced acylation, instead targeting pMLKL for degradation, resulting in cell death rescue. Figure created using BioRender. Data represent the mean error bars represent ±1 SD; $n = 3$. * represents $p < 0.05$, *** represents $p < 0.001$. (E) Proposed model for the role of zDHHC21 during necroptosis. Cells promote degradation of pMLKL in necroptosis as a way to limit cell death before being overcome with death signal. Loss of zDHHC21 results in lesser retention of pMLKL at the plasma membranes due to reduced acylation, instead targeting pMLKL for degradation resulting in cell death rescue. Figure created using BioRender.

(decrease $p < 0.001$) in the membrane-localized pMLKL (Figures 4B and S6B) in shzDHHC21 cells as compared to the control shRFP cells during necroptosis. While the reduction of plasma membrane-residing pMLKL is expected upon disruption of its acylation, the overall decrease of pMLKL under these conditions is interesting and suggests that zDHHC21 activity is important for maintaining cellular levels of pMLKL during necroptosis and that reducing zDHHC21 activity decreases cellular pMLKL levels.

Several studies suggested that MLKL and pMLKL are involved in endocytosis, cellular trafficking and exocytosis during necroptosis.[40,41] To exclude the idea that the reduction in pMLKL we observed when blocking its acylation is due to its secretion to the extracellular environment, we investigated pMLKL levels in the extracellular vesicles when zDHHC21 is inactivated. We collected cell culture media from necroptotic and control shzDHHC21 and shRFP cells and isolated the extracellular vesicles by ultracentrifugation. Necroptotic shzDHHC21 cells showed a 33% ($p < 0.01$) reduction in pMLKL, released through extracellular vesicles as compared to as shRFP necroptotic cells (Figure S6C,D), excluding increased secretion in shZDHHC21 cells to reduce cellular pMLKL levels. We note that the levels of released flotillin 1, a protein commonly associated with extracellular vesicles,[42] also decreased in necroptotic shzDHHC21 cells (18%, $p = 0.086$, Figure S6C,E) suggesting an overall reduction in extracellular components released in shzDHHC21 cells and that relative pMLKL levels remain unchanged during necroptosis (Figure 4C). Altogether, these findings clearly suggest that zDHHC21 activity plays a role in regulating cellular pMLKL levels and maintaining the integrity of the plasma membrane during necroptosis.

Reducing zDHHC21 Activity Increased pMLKL Degradation. Necroptosis involves a complex regulation of MLKL levels.[41] These include lysosomal[40] and ubiquitylation-mediated proteasomal degradation.[43] Recent studies suggest targeting proteasomal degradation of MLKL is an effective way to limit necroptotic cells death via the reduction of MLKL.[44] Our results showing that reduced zDHHC21 activity decreased cellular pMLKL levels led us to suspect the involvement of degradation pathways that might impact pMLKL levels when its membrane association is reduced. To probe the link between pMLKL acylation and proteasomal degradation in necroptosis, we treated shRFP and shzDHHC21 cells with (*R*)-MG132, a small molecular inhibitor of the proteasome.[45,46] Following treatment with (*R*)-MG132 and induction of necroptosis as we described earlier, cells were collected and analyzed using Western blotting (Figure 5A,B). We compared the effect of (*R*)-MG132 on pMLKL levels in necroptotic shzDHHC21 and necroptotic shRFP cells to assess the contribution of proteasomal degradation in pMLKL levels when its membrane

https://doi.org/10.1021/acschembio.3c00603
ACS Chem. Biol. 2024, 19, 407−418

association in reduced. We observed a 43% increase ($p < 0.05$) in pMLKL levels in necroptotic shzDHHC21 cells as compared to necroptotic shRFP cells (Figure 5B). These results suggest that the proteasomal degradation of pMLKL is increased when its acylation and membrane association is reduced. To support our observations on reduced acylation promoting pMLKL degradation, we used cycloheximide (CHX) which blocks protein translation,[47] a useful tool to study protein synthesis in cells.[48] shzDHHC21 and shRFP cells were treated with CHX prior to induction of necroptosis, and samples were collected at 0, 3, and 5 h of necroptosis (Figure 5C,D). The effect of zDHHC21 on the degradation of pMLKL in necroptosis is shown by comparing the band intensities of the proteins in shRFP and shzDHHC21 cells in the presence of CHX treatment for 3 and 5 h of necroptosis, respectively (Figure 5C). We observed similar decreases in pMLKL levels after 3 and 5 h of CHX treatment in necroptosis (Figure 5D) supporting our observation that reduced acylation of pMLKL increases its degradation. We note that MLKL has a long half-life (28 h in HeLa cells after CHX treatment[49]), which is likely responsible for its sustained levels in this experiment. Altogether, these results suggest a mechanism by which zDHHC21-mediated acylation contributes to the retention of pMLKL at the plasma membrane during necroptosis and reducing the acylation of pMLKL targets it for degradation (Figure 5E).

DISCUSSION

Studies on MLKL has gained traction in the past few years.[50] Other than its necroptotic function, not much is known about the physiological role of MLKL, although its involvement in endocytic trafficking has been recently reported.[41] It has been shown that MLKL is maintained in the cytoplasm, which then clusters at the plasma membrane under necroptotic stimuli, leading to membrane disruption.[51,52] Previous studies have highlighted the electrostatic interactions between MLKL and plasma membrane-associated PIP_2 to be an important contributor to membrane binding of MLKL during necroptosis. Adding to these known interactions, we have previously demonstrated that MLKL is acylated during necroptosis. Simulation of a nonacylated MLKL with a membrane model showed PIPs are indeed recruited to the protein binding site.[23] These results supported the dynamic interaction between MLKL and membrane lipids and suggested local membrane lipid reorganization upon MLKL binding. Here, we characterized acylation on MLKL and study the impact of acylation on the cellular fate of MLKL. We initially identified the acylation sites on MLKL. While the monoacylated MLKL is the predominant form, our results show that C184, C269, and C289 can undergo acylation, albeit one at a time, suggesting a promiscuity for the cysteine preferences. All-atom MD simulations using an acylated form of MLKL and realistic membrane models that can mimic experimentally established interactions show a particular lipid signature upon interaction with the protein, supporting that the acyl chain can cause restructuring of the membrane lipids and contribute to membrane disruption. Comparing the trajectories of acylated MLKL and membrane to our previously reported trajectories on nonacylated MLKL,[23] we observe a conserved lipid fingerprint for the individual conformations as well as distinct local rearrangements in the presence of lipid tail in the acylated form. These interactions can result in local membrane environments with different physical properties, which may affect membrane permeabilization. We believe that integrating modeling approaches with experimental data is key for generating detailed models of how the acylation of MLKL contributes to membrane permeabilization at the molecular level.

We also show that multiple *S*-acyltransferases can modify pMLKL. Among the members we tested, zDHHC21 showed the strongest effect in acylating pMLKL during necroptosis. Reducing the activity of zDHHC21 decreases the membrane association of pMLKL and restores membrane integrity during necroptosis. Further, blocking zDHHC21-mediated pMLKL acylation promoted the degradation of pMLKL, reducing the level of this key signaling protein. Based on these results, we envision a dual role for pMLKL acylation in necroptosis. First, this acylation increases the plasma membrane binding of pMLKL and exacerbates necroptosis. Second, the acylation mediated-membrane association of pMLKL prevents its degradation and reducing pMLKL acylation can increase its degradation and ameliorate necroptotic activity. Overall, these results establish previously unknown mechanisms that modulate pMLKL functioning during necroptosis.

MATERIALS

The cell lines were obtained from ATCC (HT-29 cells, HTB38, adult Caucasian female origin). For the cell culture, DMEM and penicillin/streptomycin were obtained from Corning, FBS was obtained from Sigma, and trypsin (from bovine pancreas) was obtained from Millipore Sigma (catalog no. T6567-5 × 20UG; CAS: 9002-07-7). Plasmids were obtained from Millipore Sigma (shzDHHC5 and shzDHHC21 in pLKO.1 vectors provided as bacterial glycerol stocks, shzDHHC5: NM_015457, TRCN0000162357; shzDHHC21: NM_178566, TRCN0000144923). Plasmid pLYS1-Myc for overexpression of MLKL was obtained from Dr. Yasemin Sancak; psPAX2 was a gift from Dr. Didier Trono (Addgene plasmid, cat. no. 12260); pCMV-VSV-G was a gift from Dr. Bob Weinberg (Stewart et al., 2003; Addgene plasmid, cat. no. 8854); shRFP (rfp_59s1c1; TRCN0000072205) was a gift by Dr. Yasemin Sancak, and shzDHHC20 was a gift by Dr. Eric Witze. The QuikChange II XL Site-Directed Mutagenesis Kit was obtained from Agilent Technologies (Cat. #200521). For plasmid extraction, the E.Z.N.A Plasmid DNA Mini Kit was obtained from Omega Bio-Tek (Cat. #D6945-01).

TNF-α (carrier free) was obtained from R&D Systems (Cat. #210-TA/CF), BV6 was obtained from Selleck Chemicals (Cat. #S7597; CAS: 1001600-56-1), and zVAD-FMK was obtained from Enzo Life Sciences (Cat. #ALX-260-020; CAS: 220644-02-0). Propidium iodide, Pierce Protease Inhibitor (Cat. #A32955), Pierce High Capacity Neutravidin Agarose (Cat. #29202), and M-PER Mammalian Protein Extraction Reagent (Cat. #78501) were obtained from ThermoFisher Scientific. Puromycin (cat. no. P8833; CAS: 58-58-2), Polybrene (cat. no. TR-1003), and X-treme GENE 9 transfection reagent (cat. no. XTG9-RO) were obtained from Millipore Sigma. Cycloheximide (catalog no. 14126) was obtained from Cayman Chemicals.

Antibodies were obtained from Cell Signaling Technology (rabbit monoclonal anti-MLKL, cat. no. 14993S, RRID: AB_2721822; rabbit monoclonal anti-pMLKL, Cat. #91689, RRID: AB_2732034, rabbit monoclonal anti-Myc tag, Cat. #2278, RRID: AB_490778, rabbit monoclonal anticalnexin, and cat. no. 2679S, RRID: AB_2228381), Proteintech (rabbit polyclonal anti-Flotillin 1, cat. no. 15571-1-AP, RRID: AB_2106746), Millipore Sigma (mouse monoclonal anti-α tubulin, Cat. #T9026, RRID: AB_477593), Promega (goat antirabbit HRP conjugate, cat. no. W4011, RRID: AB_430833), and Jackson Immunoresearch Lab (goat antimouse HRP conjugate, cat. no. 115-035-174, RRID: AB_2338512).

A Coomassie (Bradford) Protein Assay Kit (Cat. #23200), Pierce BCA protein assay kit (Cat. #23225), and Supersignal West Pico Chemiluminescent substrate (Cat. #34080) were obtained from

https://doi.org/10.1021/acschembio.3c00603
ACS Chem. Biol. 2024, 19, 407−418

Thermo Fisher Scientific. Fatty acid free BSA (cat. #A7030, CAS: 9048-46-8), Triton^{XM} X-100 (cat. #T9284), sodium dodecyl sulfate (SDS) (cat. #L3771, CAS: 151-21-3), azide-PEG3-biotin conjugate (cat. #762024, CAS: 875770-34-6), methoxypolyethylene glycol maleimide (mPEG) (cat. #63187, CAS: 99126-64-4), and *N*-ethylmaleimde (NEM) (cat. #E3876, CAS: 128-53-0) were obtained from MilliporeSigma. Tris(2-carboxyethyl)phosphine (TCEP) hydrochloride (Cat. #K831, CAS: 51805-45-9) was purchased from VWR. Tris[(1-benzyl-1*H*-1,2,3-triazol-4-yl)methyl]amine (TBTA) (Cat. #18816, CAS: 510758-28-8) was obtained from Cayman Chemicals.

METHODS

All-Atom Molecular Dynamics Simulations. We conducted molecular dynamics (MD) simulations of an *S*-acylated version of a single MLKL protein (PDBID:4BTF) and a membrane model with 600 lipids per leaflet. The membrane was modeled after the PM with a mixture of five lipid species, dioleoyl-phosphatidylcholine (DOPC)/cholesterol (Chol)/dioleoyl-phosphatidylethanolamine (DOPE)/palmitoyl-oleoyl-phosphatidylinositol-5-phosphate (POPI-1,5)/palmitoyl-oleoyl-phosphatidylinositol-(2,4)-bisphosphate (POPI-2,4) (40:32:20:4:4 mol %). Hereon after, POPI-1,5 and POPI-2,4 are termed PIP and PIP2. The model was built using a CHARMM-GUI Membrane Builder,[53,54] and the protein was acylated with a 24 carbons lipid tail at 280C using the Solution Builder and in-house Python scripts. The protein was initially positioned with the 280C residue facing the membrane, and the lipid tail partially inserted into the membrane. We ran three simulation replicas of the protein-membrane system with neutralizing ions for 50 ns at 310.15 K using GROMACS,[55] the CHARMM36m force field,[56−58] and an integration time of 2 fs. In each replica, the membrane lipids started from a different random distribution to ensure independent trajectories. The final configurations of these replicas were transferred to the Anton 2 machine[59] to extend the simulation for 1 μs. The pressure was maintained at 1 bar using a Parrinello−Rahman barostat[60] with an isothermal compressibility of 4.5×10^{-5} bar^{-1}, and we used the particle mesh Ewald methods to account for long-range electrostatics.[61]

Cell Culture and Culture Conditions. Human colorectal adenocarcinoma HT-29 cell (ATCC HTB-38, adult Caucasian female origin) were cultured at 37 °C in a 5% CO_2 atmosphere in DMEM supplemented with a 10% (v/v) fetal bovine serum and 1% (v/v) penicillin/streptomycin solution. Cells were cultured for approximately 2 months and routinely checked for mycoplasma infection. Cells were plated according to the requirement of each experiment, as described below. Knockdown of zDHHC5, zDHHC20, and zDHHC21 in HT-29 cells was performed as described previously.[62] For knockdown, cells were transduced with lentiviral particles packaged with shzDHHC5, shzDHHC20, shzDHHC21, and shRFP in pLKO.1-Puro vector, and stably transduced cells were selected with puromycin. For overexpression, a commercially available pLYS1-Myc vector was used and subcloned to overexpress MLKL. Lentiviral particles of the overexpression system of MLKL and MLKL mutants were packaged similarly as for knockdown.

METHOD DETAILS

Necroptosis Treatment. To induce necroptosis cell death, HT-29 cells were initially sensitized to TNF-dependent cell death pathway by SMAC mimetic BV6 (1 μM) and were cotreated with pan-caspase inhibitor zVAD-FMK (25 μM) and incubated for 30 min at 37 °C. Cells were then treated with TNF-α (10 ng/mL) and was incubated for 3 h.

(*R*)-MG132 Treatments. 8×10^6 HT-29 cells were plated in overnight. Cells were pretreated with 10 μM of (*R*)-MG132 in DMSO solution for 24 h, followed by BV6, zVAD-FMK, and TNF-α treatment. Cells were collected after 3 h of necroptosis and ultracentrifuged at 100,000 rcf for 45 min at 4 °C to separate the cytosolic proteins from the membrane proteins. The cytosolic proteins were precipitated using cold 1× PBS, ice-cold methanol, and ice-cold chloroform in a 1:2:1.5 ratio and samples were normalized based on the protein content. Samples were prepared for Western blotting and 5 μg of sample was loaded for each protein of interest.

Cycloheximide Treatments. 1.5×10^6 HT-29 cells were plated in 6-well plates overnight. Cells were treated with 300 μg/mL cycloheximide (CHX) in a DMSO solution along with BV6 and zVAD-FMK 30 min prior to addition of TNF-α. Cells were collected at 0, 3, and 5 h following necroptosis inducted, lysed, and normalized based on the protein content. Samples were prepared for Western blotting and 5 μg of sample was loaded for each protein of interest.

PI Uptake. Cells (40×10^3) were seeded in 96-well plates overnight. After the designated time, the plate was centrifuged for 2 min at 200 rcf at RT. The media was removed from each well and 200 μL of 5 μg/mL PI in a 1× PBS solution. The plate was incubated for 30 min and again centrifuged. The fluorescence was read at an excitation wavelength of 535 nm and emission wavelength of 625 nm in a Biotek Synergy H1 monochromator.

Preparation of Extracellular Vesicles. Media from the plated shRFP and shzDHHC21 control and necroptotic cells was collected and centrifuged at 300 rcf followed by 800 rcf for 30 min at 4 °C to remove cell debris. The supernatant was then filtered through a 0.2 μm filter followed by centrifugation at 100,000 rcf for 2 h. The medium was decanted, and the pellet of extracellular vesicles was lysed followed by normalization based on protein content. The samples were then prepared for Western blotting.

Generation of MLKL Mutants. The point mutations in the pLys1-MLKL-Myc plasmids were conducted using a QuikChange II XL Site-Directed Mutagenesis Kit (Agilent Technologies Cat. #200521). XL-10 Gold ultracompetent cells were used for transformation and mutated plasmids were extracted using an E.Z.N.A Plasmid DNA Mini Kit. The mutations were confirmed by Sanger sequencing using a Genewiz (Azenta Life Sciences). The primers for introducing point mutations were designed on Benchling and obtained from Integrated DNA Technologies. Sequences of primers used to introduce point mutations are provided in Table S2.

APE Procedure. APE procedure was modified based on previous protocols and has been described previously.[19]

Digital Droplet PCR. Total RNA from shzDHHC5, shzDHHC20, shzDHHC21, and shRFP cells was extracted using the E.Z.N.A Total RNA kit. RNA was converted into cDNA using a Biorad Droplet Digital PCR QX200 system with a Biorad iScript cDNA synthesis kit. cDNA was diluted 1:20 for further use with molecular grade water. Reaction mixtures for digital droplet PCR (ddPCR), including the primers and cDNA, were prepared with ddPCR Supermix for probes according to Biorad protocols and distributed in 96-well plates. A Biorad automated droplet generator was used to create water-oil emulsion droplets in a 96-well plate and subjected to PCR. The cycle was as follows: 95 °C for 10 min, followed by 40 cycles of (1) 94 °C for 30 s and (2) 56 °C for 60 s, with a final 10 min inactivation step at 98 °C. The plate was read using a QX200 droplet reader, which measured and quantified the fluorescence from the FAM fluorophore of the amplified target gene and the HEX fluorophore of the reference gene (HPRT1). Biorad Quantasoft software was used for the data analysis and visualization of the data. The changes in the gene expression and *p* values were calculated relative to HPRT1.

https://doi.org/10.1021/acschembio.3c00603
ACS Chem. Biol. 2024, 19, 407−418

The sequences for primers and probes are provided in Table S3.

Western Blotting. Samples were loaded and separated with sodium dodecyl sulfate polyacrylamide gel (8 or 10%) electrophoresis at 150 V. Methanol activated poly(vinyl difluoride) (PVDF) membranes were used. The separated proteins were transferred onto the PVDF membranes at 50 V for 2 h. Blocking conditions were incubation with 10% nonfat dry milk in tris-buffered saline (TBS)-Tween [10 mM Tris-base, 100 mM NaCl, 0.1% Tween 20 (pH 7.5)] at RT for 1 h. Membranes were washed four times at 7 min intervals in TBS-Tween. The corresponding membranes were incubated overnight at 4 °C with primary antibodies (1:500/1:1000 for Myc-tag, 1:2000 dilution for MLKL, 1:500 for pMLKL, 1:10,000 for flotillin 1, 1:10,000 for calnexin, and 1:5000 for α-tubulin). After incubation, the membranes were then washed four times with TBS-Tween for 10 min each time. Dilutions for antirabbit and antimouse secondary antibodies were 1:2000 in 5% nonfat dry milk in TBS-Tween, followed by incubation at RT for 1 h. The membranes were washed as earlier followed by developing with the Super Signal West Pico kit.

Quantification of Western Blots. Fiji software was used for the quantification of the Western blots. Samples for all Western blot quantifications were loaded in triplicate. A frame for the measurement was developed by using the rectangle tool of Fiji to cover the largest band of the protein of interest. The intensities of the other protein bands were similarly obtained. The background was also measured with the same frame to obtain background intensity measurements. The measured intensities from the protein of interest and background were then inverted by deducting measurements from 255. 255 is the pixel value assigned to the white background. The inverted intensities of the protein bands of interest were corrected with the inverted intensities of the background. For APE blots, the relative intensities were obtained by dividing the corrected intensities of migrated bands by that of the nonmigrated bands. For all other Western blots, the relative intensities were obtained by dividing the corrected intensity of MLKL or pMLKL by the corrected intensity of the loading control, such as calnexin or tubulin. The calculations for every quantification are described in the respective figure legends.

QUANTIFICATION AND STATISTICAL ANALYSIS

All statistical analysis for the Western blot quantifications, cell viability experiments, and proteomics were performed using the unpaired Student's *t*-test. p values and numbers of replicates in all figures are indicated in figure legends, where $^{***}p < 0.001$, $^{**}p < 0.01$, $^{*}p < 0.05$, and ns is $p > 0.05$.

ASSOCIATED CONTENT

Supporting Information

The Supporting Information is available free of charge at https://pubs.acs.org/doi/10.1021/acschembio.3c00603.

Amino acid sequence comparison of human and mouse MLKL, additional Western blots of control samples and blots used for quantification, bar plots supporting computational studies and additional quantifications, cysteine occupancy data from computational experiments, and primer sequences used for point mutations and gene expression studies (PDF)

AUTHOR INFORMATION

Corresponding Author

G. Ekin Atilla-Gokcumen − *Department of Chemistry, University at Buffalo, The State University of New York, Buffalo, New York 14260, United States;* orcid.org/0000-0002-7132-3873; Email: ekinatil@buffalo.edu

Authors

Apoorva J. Pradhan − *Department of Chemistry, University at Buffalo, The State University of New York, Buffalo, New York 14260, United States*

Shweta Chitkara − *Department of Chemistry, University at Buffalo, The State University of New York, Buffalo, New York 14260, United States*

Ricardo X. Ramirez − *Department of Chemical and Biological Engineering, University at Buffalo, The State University of New York, Buffalo, New York 14260, United States*

Viviana Monje-Galvan − *Department of Chemical and Biological Engineering, University at Buffalo, The State University of New York, Buffalo, New York 14260, United States;* orcid.org/0000-0002-9202-782X

Yasemin Sancak − *Department of Pharmacology, University of Washington, Seattle, Washington 98195, United States*

Complete contact information is available at: https://pubs.acs.org/10.1021/acschembio.3c00603

Author Contributions

Experiments were designed by A.J.P., S.C., V.M.-G., Y.S., and G.E.A.-G. The experiments were conducted by A.J.P., S.C., and Y.S. The all-atom molecular dynamic simulations were conducted by R.X.R. and V.M.-G. The manuscript was written by A.J.P., R.X.R., V.M.-G., and G.E.A.-G. The study was directed by G.E.A.-G. The authors declare no conflict of interest.

Notes

The authors declare no competing financial interest.

ACKNOWLEDGMENTS

We acknowledge the support from the National Science Foundation grant (MCB1817468 to G.E.A.G.) and The Research Foundation, The State University of New York (#1181362). We are grateful for the support from Dr. Marjorie Winkler Professorship. We thank Eric Witze for sharing zDHHC20 knockdown plasmid. Simulations were run in part at the University at Buffalo's Center for Computational Research[63] and in the Anton 2 machine. Anton 2 computer time was provided by the Pittsburgh Supercomputing Center (PSC) through Grant R01GM116961 from the National Institutes of Health, specific award MCB200093P. The Anton 2 machine as PSC was generously made available by D.E. Shaw Research.[59]

REFERENCES

(1) Green, D. R. Cell Death in Development. *Cold Spring Harbor Perspect. Biol.* **2022**, *14* (4), a041095.

(2) Gibellini, L.; Moro, L. Programmed Cell Death in Health and Disease. *Cells* **2021**, *10* (7), 1765.

(3) Vandenabeele, P.; Galluzzi, L.; Vanden Berghe, T.; Kroemer, G. Molecular mechanisms of necroptosis: an ordered cellular explosion. *Nat. Rev. Mol. Cell Biol.* **2010**, *11* (10), 700−714.

(4) Kaczmarek, A.; Vandenabeele, P.; Krysko, D. V. Necroptosis: the release of damage-associated molecular patterns and its physiological relevance. *Immunity* **2013**, *38* (2), 209−223.

(5) Molnár, T.; Mázló, A.; Tslaf, V.; Söllősi, A. G.; Emri, G.; Koncz, G. Current translational potential and underlying molecular mechanisms of necroptosis. *Cell Death Dis.* **2019**, *10* (11), 860.
(6) Gough, P.; Myles, I. A. Tumor Necrosis Factor Receptors: Pleiotropic Signaling Complexes and Their Differential Effects. *Front. Immunol.* **2020**, *11*, 585880.
(7) Murphy, J. M.; Czabotar, P. E.; Hildebrand, J. M.; Lucet, I. S.; Zhang, J. G.; Alvarez-Diaz, S.; Lewis, R.; Lalaoui, N.; Metcalf, D.; Webb, A. I.; et al. The pseudokinase MLKL mediates necroptosis via a molecular switch mechanism. *Immunity* **2013**, *39* (3), 443−453.
(8) Wang, H.; Sun, L.; Su, L.; Rizo, J.; Liu, L.; Wang, L. F.; Wang, F. S.; Wang, X. Mixed lineage kinase domain-like protein MLKL causes necrotic membrane disruption upon phosphorylation by RIP3. *Mol. Cell* **2014**, *54* (1), 133−146.
(9) Chen, X.; Li, W.; Ren, J.; Huang, D.; He, W. T.; Song, Y.; Yang, C.; Li, W.; Zheng, X.; Chen, P.; et al. Translocation of mixed lineage kinase domain-like protein to plasma membrane leads to necrotic cell death. *Cell Res.* **2014**, *24* (1), 105−121.
(10) Liu, S.; Liu, H.; Johnston, A.; Hanna-Addams, S.; Reynoso, E.; Xiang, Y.; Wang, Z. MLKL forms disulfide bond-dependent amyloid-like polymers to induce necroptosis. *Proc. Natl. Acad. Sci. U.S.A.* **2017**, *114* (36), No. E7450.
(11) Dondelinger, Y.; Declercq, W.; Montessuit, S.; Roelandt, R.; Goncalves, A.; Bruggeman, I.; Hulpiau, P.; Weber, K.; Sehon, C. A.; Marquis, R. W.; et al. MLKL compromises plasma membrane integrity by binding to phosphatidylinositol phosphates. *Cell Rep.* **2014**, *7* (4), 971−981.
(12) Quarato, G.; Guy, C. S.; Grace, C. R.; Llambi, F.; Nourse, A.; Rodriguez, D. A.; Wakefield, R.; Frase, S.; Moldoveanu, T.; Green, D. R. Sequential Engagement of Distinct MLKL Phosphatidylinositol-Binding Sites Executes Necroptosis. *Mol. Cell* **2016**, *61* (4), 589−601.
(13) Su, L.; Quade, B.; Wang, H.; Sun, L.; Wang, X.; Rizo, J. A plug release mechanism for membrane permeation by MLKL. *Structure* **2014**, *22* (10), 1489−1500.
(14) Davies, K. A.; Tanzer, M. C.; Griffin, M. D. W.; Mok, Y. F.; Young, S. N.; Qin, R.; Petrie, E. J.; Czabotar, P. E.; Silke, J.; Murphy, J. M. The brace helices of MLKL mediate interdomain communication and oligomerisation to regulate cell death by necroptosis. *Cell Death Differ.* **2018**, *25* (9), 1567−1580.
(15) Petrie, E. J.; Sandow, J. J.; Jacobsen, A. V.; Smith, B. J.; Griffin, M. D. W.; Lucet, I. S.; Dai, W.; Young, S. N.; Tanzer, M. C.; Wardak, A.; et al. Conformational switching of the pseudokinase domain promotes human MLKL tetramerization and cell death by necroptosis. *Nat. Commun.* **2018**, *9* (1), 2422.
(16) Hildebrand, J. M.; Tanzer, M. C.; Lucet, I. S.; Young, S. N.; Spall, S. K.; Sharma, P.; Pierotti, C.; Garnier, J.-M.; Dobson, R. C. J.; Webb, A. I.; et al. Activation of the pseudokinase MLKL unleashes the four-helix bundle domain to induce membrane localization and necroptotic cell death. *Proc. Natl. Acad. Sci. U.S.A.* **2014**, *111* (42), 15072−15077.
(17) Zhang, Y.; Liu, J.; Yu, D.; Zhu, X.; Liu, X.; Liao, J.; Li, S.; Wang, H. The MLKL kinase-like domain dimerization is an indispensable step of mammalian MLKL activation in necroptosis signaling. *Cell Death Dis.* **2021**, *12* (7), 638.
(18) Guillou, H.; Zadravec, D.; Martin, P. G. P.; Jacobsson, A. The key roles of elongases and desaturases in mammalian fatty acid metabolism: Insights from transgenic mice. *Prog. Lipid Res.* **2010**, *49* (2), 186−199.
(19) Pradhan, A. J.; Lu, D.; Parisi, L. R.; Shen, S.; Berhane, I. A.; Galster, S. L.; Bynum, K.; Monje-Galvan, V.; Gokcumen, O.; Chemler, S. R.; et al. Protein acylation by saturated very long chain fatty acids and endocytosis are involved in necroptosis. *Cell Chem. Biol.* **2021**, *28* (9), 1298.
(20) Petrie, E. J.; Birkinshaw, R. W.; Koide, A.; Denbaum, E.; Hildebrand, J. M.; Garnish, S. E.; Davies, K. A.; Sandow, J. J.; Samson, A. L.; Gavin, X.; et al. Identification of MLKL membrane translocation as a checkpoint in necroptotic cell death using Monobodies. *Proc. Natl. Acad. Sci. U.S.A.* **2020**, *117* (15), 8468−8475.
(21) Sun, L.; Wang, H.; Wang, Z.; He, S.; Chen, S.; Liao, D.; Wang, L.; Yan, J.; Liu, W.; Lei, X.; et al. Mixed lineage kinase domain-like protein mediates necrosis signaling downstream of RIP3 kinase. *Cell* **2012**, *148* (1−2), 213−227.
(22) Huang, D.; Zheng, X.; Wang, Z. A.; Chen, X.; He, W. T.; Zhang, Y.; Xu, J. G.; Zhao, H.; Shi, W.; Wang, X.; et al. The MLKL Channel in Necroptosis Is an Octamer Formed by Tetramers in a Dyadic Process. *Mol. Cell. Biol.* **2017**, *37* (5), No. e00497.
(23) Ramirez, R. X.; Campbell, O.; Pradhan, A. J.; Atilla-Gokcumen, G. E.; Monje-Galvan, V. Modeling the molecular fingerprint of protein-lipid interactions of MLKL on complex bilayers. *Front. Chem.* **2023**, *10*, 1088058.
(24) Blanc, M.; David, F. P. A.; van der Goot, F. G. SwissPalm 2: Protein S-Palmitoylation Database. *Methods Mol. Biol.* **2019**, *2009*, 203−214.
(25) Blanc, M.; David, F.; Abrami, L.; Migliozzi, D.; Armand, F.; Bürgi, J.; van der Goot, F. G. SwissPalm: Protein Palmitoylation database. *F1000Res.* **2015**, *4*, 261.
(26) Lu, D.; Parisi, L. R.; Gokcumen, O.; Atilla-Gokcumen, G. E. SREBP activation contributes to fatty acid accumulations in necroptosis. *RSC Chem. Biol.* **2023**, *4* (4), 310−322.
(27) Parisi, L. R.; Sowlati-Hashjin, S.; Berhane, I. A.; Galster, S. L.; Carter, K. A.; Lovell, J. F.; Chemler, S. R.; Karttunen, M.; Atilla-Gokcumen, G. E. Membrane Disruption by Very Long Chain Fatty Acids during Necroptosis. *ACS Chem. Biol.* **2019**, *14* (10), 2286−2294.
(28) Percher, A.; Thinon, E.; Hang, H. Mass-Tag Labeling Using Acyl-PEG Exchange for the Determination of Endogenous Protein S-Fatty Acylation. *Curr. Protoc. Protein Sci.* **2017**, *89*, 14 17 11.
(29) Sethi, A.; Horne, C. R.; Fitzgibbon, C.; Wilde, K.; Davies, K. A.; Garnish, S. E.; Jacobsen, A. V.; Samson, A. L.; Hildebrand, J. M.; Wardak, A.; et al. Membrane permeabilization is mediated by distinct epitopes in mouse and human orthologs of the necroptosis effector, MLKL. *Cell Death Differ.* **2022**, *29* (9), 1804−1815.
(30) Monje-Galvan, V.; Voth, G. A. Binding mechanism of the matrix domain of HIV-1 gag on lipid membranes. *eLife.* **2020**, *9*, No. e58621.
(31) Samal, A. B.; Green, T. J.; Saad, J. S. Atomic view of the HIV-1 matrix lattice; implications on virus assembly and envelope incorporation. *Proc. Natl. Acad. Sci. U.S.A.* **2022**, *119* (23), No. e2200794119.
(32) Banerjee, P.; Monje-Galvan, V.; Voth, G. A. Cooperative Membrane Binding of HIV-1 Matrix Proteins. *bioRxiv* **2023**.
(33) Jiang, H.; Zhang, X.; Chen, X.; Aramsangtienchai, P.; Tong, Z.; Lin, H. Protein Lipidation: Occurrence, Mechanisms, Biological Functions, and Enabling Technologies. *Chem. Rev.* **2018**, *118* (3), 919−988.
(34) Ohno, Y.; Kihara, A.; Sano, T.; Igarashi, Y. Intracellular localization and tissue-specific distribution of human and yeast DHHC cysteine-rich domain-containing proteins. *Biochim. Biophys. Acta* **2006**, *1761* (4), 474−483.
(35) Fernández-Hernando, C.; Fukata, M.; Bernatchez, P. N.; Fukata, Y.; Lin, M. I.; Bredt, D. S.; Sessa, W. C. Identification of Golgi-localized acyl transferases that palmitoylate and regulate endothelial nitric oxide synthase. *J. Cell Biol.* **2006**, *174* (3), 369−377.
(36) Runkle, K. B.; Kharbanda, A.; Stypulkowski, E.; Cao, X. J.; Wang, W.; Garcia, B. A.; Witze, E. S. Inhibition of DHHC20-Mediated EGFR Palmitoylation Creates a Dependence on EGFR Signaling. *Mol. Cell* **2016**, *62* (3), 385−396.
(37) Ko, P. J.; Woodrow, C.; Dubreuil, M. M.; Martin, B. R.; Skouta, R.; Bassik, M. C.; Dixon, S. J. A ZDHHC5-GOLGA7 Protein Acyltransferase Complex Promotes Nonapoptotic Cell Death. *Cell Chem. Biol.* **2019**, *26* (12), 1716.
(38) Yang, X.; Zheng, E.; Ma, Y.; Chatterjee, V.; Villalba, N.; Breslin, J. W.; Liu, R.; Wu, M. H.; Yuan, S. Y. DHHC21 deficiency attenuates renal dysfunction during septic injury. *Sci. Rep.* **2021**, *11* (1), 11146.
(39) Beard, R. S.; Yang, X.; Meegan, J. E.; Overstreet, J. W.; Yang, C. G. Y.; Elliott, J. A.; Reynolds, J. J.; Cha, B. J.; Pivetti, C. D.; Mitchell, D. A.; et al. Palmitoyl acyltransferase DHHC21 mediates endothelial

https://doi.org/10.1021/acschembio.3c00603
ACS Chem. Biol. 2024, 19, 407−418

dysfunction in systemic inflammatory response syndrome. *Nat. Commun.* **2016**, *7* (1), 12823.
(40) Fan, W.; Guo, J.; Gao, B.; Zhang, W.; Ling, L.; Xu, T.; Pan, C.; Li, L.; Chen, S.; Wang, H.; et al. Flotillin-mediated endocytosis and ALIX-syntenin-1-mediated exocytosis protect the cell membrane from damage caused by necroptosis. *Sci. Signaling* **2019**, *12* (583), No. eaaw3423.
(41) Yoon, S.; Kovalenko, A.; Bogdanov, K.; Wallach, D. MLKL, the Protein that Mediates Necroptosis, Also Regulates Endosomal Trafficking and Extracellular Vesicle Generation. *Immunity* **2017**, *47* (1), 51.
(42) Meister, M.; Tikkanen, R. Endocytic Trafficking of Membrane-Bound Cargo: A Flotillin Point of View. *Membranes* **2014**, *4* (3), 356−371.
(43) Yoon, S.; Bogdanov, K.; Wallach, D. Site-specific ubiquitination of MLKL targets it to endosomes and targets Listeria and Yersinia to the lysosomes. *Cell Death Differ.* **2022**, *29* (2), 306−322.
(44) Liu, Z.; Dagley, L. F.; Shield-Artin, K.; Young, S. N.; Bankovacki, A.; Wang, X.; Tang, M.; Howitt, J.; Stafford, C. A.; Nachbur, U.; et al. Oligomerization-driven MLKL ubiquitylation antagonizes necroptosis. *EMBO J.* **2021**, *40* (23), No. e103718.
(45) Kisselev, A. F.; Goldberg, A. L. Proteasome inhibitors: from research tools to drug candidates. *Chem. Biol.* **2001**, *8* (8), 739−758.
(46) Lee, D. H.; Goldberg, A. L. Proteasome inhibitors: valuable new tools for cell biologists. *Trends Cell Biol.* **1998**, *8* (10), 397−403.
(47) Schneider-Poetsch, T.; Ju, J.; Eyler, D. E.; Dang, Y.; Bhat, S.; Merrick, W. C.; Green, R.; Shen, B.; Liu, J. O. Inhibition of eukaryotic translation elongation by cycloheximide and lactimidomycin. *Nat. Chem. Biol.* **2010**, *6* (3), 209−217.
(48) Dai, C. L.; Shi, J.; Chen, Y.; Iqbal, K.; Liu, F.; Gong, C. X. Inhibition of protein synthesis alters protein degradation through activation of protein kinase B (AKT). *J. Biol. Chem.* **2013**, *288* (33), 23875−23883.
(49) Zhao, X. M.; Chen, Z.; Zhao, J. B.; Zhang, P. P.; Pu, Y. F.; Jiang, S. H.; Hou, J. J.; Cui, Y. M.; Jia, X. L.; Zhang, S. Q. Hsp90 modulates the stability of MLKL and is required for TNF-induced necroptosis. *Cell Death Dis.* **2016**, *7* (2), No. e2089-e2089.
(50) Murphy, J. M. The Killer Pseudokinase Mixed Lineage Kinase Domain-Like Protein (MLKL). *Cold Spring Harbor Perspect. Biol.* **2020**, *12* (8), a036376.
(51) Hildebrand, J. M.; Kauppi, M.; Majewski, I. J.; Liu, Z.; Cox, A. J.; Miyake, S.; Petrie, E. J.; Silk, M. A.; Li, Z.; Tanzer, M. C.; et al. A missense mutation in the MLKL brace region promotes lethal neonatal inflammation and hematopoietic dysfunction. *Nat. Commun.* **2020**, *11* (1), 3150.
(52) Samson, A. L.; Zhang, Y.; Geoghegan, N. D.; Gavin, X. J.; Davies, K. A.; Mlodzianoski, M. J.; Whitehead, L. W.; Frank, D.; Garnish, S. E.; Fitzgibbon, C.; et al. MLKL trafficking and accumulation at the plasma membrane control the kinetics and threshold for necroptosis. *Nat. Commun.* **2020**, *11* (1), 3151.
(53) Lee, J.; Patel, D. S.; Ståhle, J.; Park, S. J.; Kern, N. R.; Kim, S.; Lee, J.; Cheng, X.; Valvano, M. A.; Holst, O.; et al. CHARMM-GUI Membrane Builder for Complex Biological Membrane Simulations with Glycolipids and Lipoglycans. *J. Chem. Theory Comput.* **2019**, *15* (1), 775−786.
(54) Jo, S.; Lim, J. B.; Klauda, J. B.; Im, W. CHARMM-GUI Membrane Builder for mixed bilayers and its application to yeast membranes. *Biophys. J.* **2009**, *97* (1), 50−58.
(55) Abraham, M. J.; Murtola, T.; Schulz, R.; Páll, S.; Smith, J. C.; Hess, B.; Lindahl, E. GROMACS: High performance molecular simulations through multi-level parallelism from laptops to supercomputers. *SoftwareX* **2015**, *1−2*, 19−25.
(56) Klauda, J. B.; Venable, R. M.; Freites, J. A.; O'Connor, J. W.; Tobias, D. J.; Mondragon-Ramirez, C.; Vorobyov, I.; MacKerell, A. D.; Pastor, R. W. Update of the CHARMM All-Atom Additive Force Field for Lipids: Validation on Six Lipid Types. *J. Phys. Chem. B* **2010**, *114* (23), 7830−7843.
(57) Huang, J.; Rauscher, S.; Nawrocki, G.; Ran, T.; Feig, M.; de Groot, B. L.; Grubmüller, H.; MacKerell, A. D. CHARMM36m: an improved force field for folded and intrinsically disordered proteins. *Nat. Methods* **2017**, *14* (1), 71−73.
(58) Vanommeslaeghe, K.; MacKerell, A. D. Automation of the CHARMM General Force Field (CGenFF) I: Bond Perception and Atom Typing. *J. Chem. Inf. Model.* **2012**, *52* (12), 3144−3154.
(59) Shaw, D. E.; Grossman, J. P.; Bank, J. A.; Batson, B.; Butts, J. A.; Chao, J. C.; Deneroff, M. M.; Dror, R. O.; Even, A.; Fenton, C. H.; et al. Anton 2: Raising the Bar for Performance and Programmability in a Special-Purpose Molecular Dynamics Supercomputer. *SC '14: Proceedings of the International Conference for High Performance Computing, Networking, Storage and Analysis*, 2014; pp 41−53..
(60) Parrinello, M.; Rahman, A. Polymorphic transitions in single crystals: A new molecular dynamics method. *J. Appl. Phys.* **1981**, *52* (12), 7182−7190.
(61) Darden, T.; York, D.; Pedersen, L. Particle mesh Ewald: An N·log(N) method for Ewald sums in large systems. *J. Chem. Phys.* **1993**, *98* (12), 10089−10092.
(62) Parisi, L. R.; Li, N.; Atilla-Gokcumen, G. E. Very Long Chain Fatty Acids Are Functionally Involved in Necroptosis. *Cell Chem. Biol.* **2017**, *24* (12), 1445.
(63) Center for Computational Research UaB. *CCR Facility Description*, 2019. https://ubir.buffalo.edu/xmlui/handle/10477/79221.

https://doi.org/10.1021/acschembio.3c00603
ACS Chem. Biol. 2024, 19, 407−418